ELSEVIER

# Large-eddy simulation of a concave wall boundary layer

**Thomas S. Lund and Parviz Moin**
Center for Turbulence Research, Stanford University, Stanford, CA, USA

Large-eddy simulations (LESs) of a spatially evolving boundary layer on a concave surface are discussed. A second-order finite-difference method with a fully implicit time advancement scheme is used to integrate the incompressible Navier–Stokes equations. The dynamic subgrid-scale model is used to account for the effects of the unresolved turbulent motions. The simulations attempt to duplicate a set of laboratory experiments conducted at a momentum thickness Reynolds number of 1300. The simulation results generally compare well with the experimental data and accurately predict the structural changes that result from the destabilizing effect of concave curvature. Some discrepancies exist with the experimental data, and these appear to be related in part to the details of the turbulent inflow data used in the simulations. Slightly better agreement with the experimental data is obtained if inflow data with higher fluctuation levels and artificially enhanced streamwise coherence is used. The sensitivity to inflow conditions appears to be related to the amplification of existing structures within the curved section of the domain. The simulation using inflow data with enhanced streamwise coherence is shown to lead to the formation of distinct Taylor–Görtler vortices; whereas, the other simulations lead to a variety of weaker, less-developed secondary flow patterns. These results seem to suggest that the upstream flow history can exert a significant influence on the initial development of secondary flow structures in concave turbulent boundary layer flows.

**Keywords:** large-eddy simulation; concave curvature; Taylor–Görtler vortices; boundary layer; turbulent flow

## Introduction

Turbulence modeling continues to be one of the most difficult problems in fluid mechanics. Existing prediction methods are well developed for certain classes of simple equilibrium flows, but are still not entirely satisfactory for a large category of complex nonequilibrium flows found in engineering practice. Direct and large-eddy simulation (LES) approaches have long been believed to have great potential for the accurate prediction of difficult turbulent flows, but the associated computational cost has been prohibitive for practical problems. This remains true for direct simulation, but is no longer the case for large-eddy simulation. Advances in computer hardware, numerical methods, and subgrid-scale modeling have made it possible to conduct LES for flows of practical interest at Reynolds numbers in the range of laboratory experiments. A handful of these simulations have been performed over the last few years (cf. Akselvoll and Moin 1993; Zang et al. 1993; He and Song 1993). Many of these recent simulations were performed to develop LES technology for complex flows and to assess the accuracy of the dynamic subgrid-scale model. The indication from these first simulations is that LES in conjunction with the dynamic model is capable of accurately predicting high-Reynolds number complex flows for which Reynolds-averaged techniques have not been able to produce satisfactory results. The validation and technology development phase for LES of complex flows is ongoing, and additional challenging test cases must be attempted. The objective of this work is to apply LES and the dynamic subgrid-scale model to the flow of a boundary layer over a concave surface.

Although the geometry of a concave wall is not very complex, the boundary layer that develops on its surface is difficult to model due to the presence of streamwise Taylor–Görtler vortices. These vortices arise as a result of a centrifugal instability associated with concave curvature. The vortices are of the same scale as the boundary-layer thickness, alternate in sense of rotation, and are strong enough to induce significant changes in the boundary layer statistics. Owing to their streamwise orientation and alternate signs, the Taylor-Görtler vortices induce alternating bands of flow toward and away from the wall. The induced upwash and downwash motions serve as effective agents to transport streamwise momentum normal to the wall, thereby increasing the skin friction. Reynolds-averaged prediction techniques are unable to resolve these vortices and must resort to ad hoc correction terms. Aside from Taylor–Görtler vortices, concave curvature affects the turbulent Reynolds stress budget through supplemental production terms. This effect is captured in full Reynolds stress models but is absent in the more commonly used algebraic, one- or two-equation models.

In contrast to Reynolds-averaged approaches, LES is well suited for the concave-wall boundary-layer flow, since the Taylor–Görtler vortices are simulated directly. In addition, the effects of curvature, not associated with vortices, are captured.

Address reprint requests to T. S. Lund, Center for Turbulence Research, Stanford University, Stanford CA 94305-3030.

Received 27 October 1995; accepted 17 February 1996

Int. J. Heat and Fluid Flow 17: 290–295, 1996

655 Avenue of the Americas, New York, NY 10010

0142-727X/96/$15.00
PII S0142-727X(96)00039-2

The simulations reported here are designed to match the laboratory conditions of Barlow and Johnston (1988) and Johnson and Johnston (1989). These experiments are an ideal test case, since a rather complete set of velocity statistics are available for several streamwise stations.

## Numerical method

The computer code used for this project is based on the second-order staggered-mesh finite-difference algorithm described by Choi et al. (1993). The incompressible Navier–Stokes equations are integrated in time with a fully implicit variant of the fractional step algorithm. Generalized curvilinear coordinates are used in two directions with the third direction (usually spanwise) restricted to be uniform. In the fractional step procedure, the dependent variables are advanced in a two-step process where an intermediate velocity field is first advanced without the pressure gradient term. The effect of the pressure gradient is then accounted for through a correction term obtained by solving a Poisson equation. In the current implementation, the intermediate velocity field is advanced with a fully-implicit scheme where Newton iteration is used to reduce the factorization error. By taking a Fourier transform in the uniform mesh direction (spanwise), the Poisson equation is reduced to a series of two-dimensional (2-D) problems, one for each spanwise wave number. The lowest wave number system is solved with a direct inversion technique; whereas, the higher wave number systems are treated with a Gauss–Seidel iteration scheme. Although the scheme is stable for CFL numbers of at least 5, the time-step is usually dictated by accuracy requirements. In this work, the maximum Courant-Friedrichs-Lewy number (CFL) is held below 2.0.

## Computational domain and flow conditions

The simulations attempt to duplicate the laboratory experiments conducted by Barlow and Johnston (1988) and Johnson and Johnston (1989). The experimental facility is a water channel where a straight entry flow section is fitted to a 90° constant radius of curvature bend (see Figure 1). The convex wall deviates slightly from a circular arc in order to minimize the streamwise pressure gradient on the concave wall. Boundary layers develop on both channel walls; one experiences an abrupt transition to concave curvature, while the other experiences a transition to convex curvature. Measurements are available only for the concave side. Both boundary layers are tripped early on the entry section and become fully turbulent by the beginning of the curved section. At this station, the two boundary layers are separated by about 1.5 boundary-layer thicknesses of potential core in the center of the channel. The potential region diminishes with downstream distance, and the two boundary layers merge between the 75 and 90° stations. The momentum thickness Reynolds number at the beginning of the curve is $R_{\theta_0} = 1300$. At this station, the ratio of boundary-layer thickness to radius of curvature, to $\delta_0/R$, is 0.055, which is sufficiently large to create significant curvature effects.

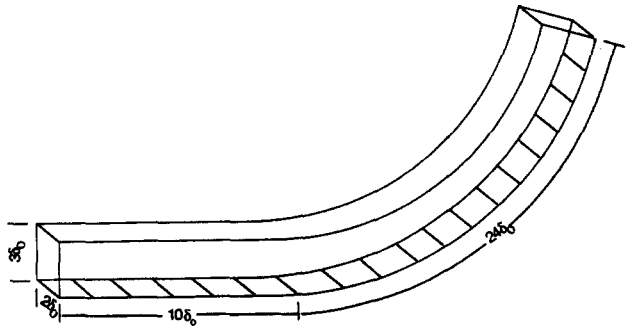


*Figure 1* Computational domain; all dimensions are referred to the boundary-layer thickness measured at the location where the curvature begins ($\delta_0$); the radius of curvature is $R = 18.1\delta_0$

The computational domain is an abbreviated version of the experimental geometry. A sketch is provided in Figure 1. The calculation begins approximately 10 boundary-layer thicknesses upstream of the curved section and ends at the 75° station (the boundary-layer thickness measured at the onset of curvature, $\delta_0$ is used as the normalizing length scale throughout). Unsteady turbulent boundary-layer data are supplied at the inflow boundary; whereas, a convective boundary condition is used at the outflow boundary. The domain extends $2\delta_0$ in the spanwise direction, and periodic boundary conditions are used. According to the experimental measurements, the spanwise width is sufficient to enclose two to four streamwise Taylor–Görtler vortices. Only the concave boundary layer is simulated, and consequently the domain extends from the concave wall to the stream surface that lies along the channel centerline. No-slip conditions are applied at the solid wall; whereas, impermeable and no-stress conditions are applied at the upper boundary. The position of the streamline boundary was determined by conducting an inviscid analysis of the experimental geometry. The displacement effects of both boundary layers was accounted for in this analysis.

The computational grid contains $358 \times 44 \times 64$ points in the streamwise, wall-normal, and spanwise directions respectively. The mesh is stretched in the wall-normal direction and uniform

## Notation

| | |
|---|---|
| $C_f$ | skin friction coefficient, $(\nu\, \partial u/\partial y\|_{\text{wall}})/(0.5\rho U_\infty^2)$ |
| $C_p$ | pressure coefficient, $(p - p_{\text{ref}})/(0.5\rho U_\infty^2)$ |
| $p$ | static pressure |
| $p_{\text{ref}}$ | reference pressure (taken at the first experimental measurement location on the flat entry section) |
| $R$ | Radius of curvature (constant in the test section) |
| $R_{\theta_0}$ | momentum thickness Reynolds number at the start of the curve, $(U_\infty \theta_0)/\nu$ |
| $U_p(y)$ | inviscid velocity profile in the curved section, Equation 1 |
| $U_{pw}$ | inviscid velocity at the concave wall |
| $U_\infty$ | boundary-layer edge velocity upstream of the curve |
| $u'$ | streamwise velocity fluctuation |
| $v'$ | wall-normal velocity fluctuation |
| $w'$ | spanwise velocity fluctuation |
| $X_l$ | streamwise length of the computational domain |
| $x$ | streamwise coordinate |
| $y$ | wall-normal coordinate |
| $z$ | spanwise coordinate |

*Greek*

| | |
|---|---|
| $\delta$ | boundary-layer thickness |
| $\delta_0$ | boundary-layer thickness at the start of the curve |
| $\theta_0$ | momentum thickness at the start of the curve |
| $\nu$ | kinematic viscosity |
| $\rho$ | density |

in the other two. The grid spacings, based on wall units at the location where the curve begins, are $\Delta x^+ = 50$, $\Delta y^+_{min} = 1$, and $\Delta z^+ = 16$.

## Inflow boundary data

A spatially evolving simulation such as this one requires the specification of instantaneous turbulent data at the inflow boundary. Accurate inflow data is required to ensure that the boundary layer is fully turbulent and in equilibrium at the beginning of the curve. Instantaneous inflow data are generated via an auxiliary large-eddy simulation of a flat plate boundary layer. This simulation is also spatially evolving, but makes use of Spalart's method (1988) to generate its own inflow data by resealing the data at the exit station (see Wu et al. (1995) for more details on the inflow generation). The resolution of the inflow simulation is identical to that of the main simulation. The inflow simulation is run in parallel with the main simulation in a time-synchronous fashion. At each time-step, the velocity field is extracted from an appropriate $y$–$z$ plane in the inflow simulation. These data are used directly as the inflow boundary conditions. In practice, the inflow simulation can be either run at the same time as the main simulation or run ahead of time and the inflow data stored on disk. The inflow simulation increases the overall cost of the main simulation by about 10%.

## Simulation results

Before sampling statistics, the simulation is run for an initial transient elimination period of 45 boundary layer inertial time scale units ($\delta_0/U_\infty$), or equivalently 1.2 flow-through times ($X_l/U_\infty$). Statistics are then sampled over a period of 150 inertial time scales (3.9 flow-through times). Mean quantities are formed by averaging over both the spanwise direction and time.

The pressure distribution on the concave wall is compared with the experimental measurements in Figure 2. The curve begins at $x = 0$, and, thus, negative values of $x$ correspond to the flat entry section. The pressure is reasonably constant with the only non-negligible gradient occurring near the start of the curve. This is due to slight errors in the contour applied to the upper domain boundary. Since the streamsurface was determined through an inviscid analysis of the experimental configuration, it is quite likely that a similar pressure signature exists in the experiment. Unfortunately, no detailed experimental measurements are a available in the region near the start of the curve.

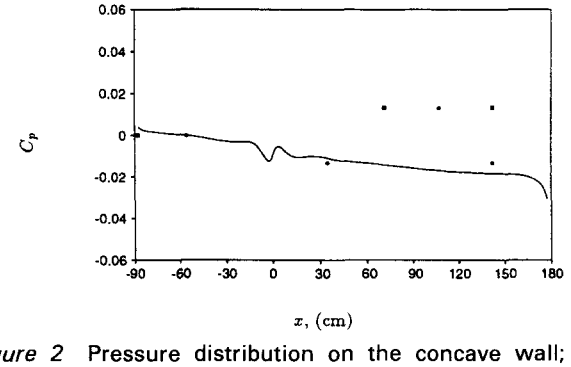


*Figure 2* Pressure distribution on the concave wall; the curve begins at $x=0$; $\delta_0$ is the boundary-layer thickness at $x=0$; ——, LES; ●, Johnson and Johnston (1989); ■, Barlow and Johnston (1988); in the experiments, the pressure is determined indirectly from the velocity measured in the potential core region

The maximum deviation from uniform pressure is roughly 2%, which probably has a small effect on the boundary-layer development. Aside from the pressure variation near the start of the curve, there is a small uniform drop in pressure with streamwise distance. This is due to a slight acceleration of the core flow resulting from errors made in the estimate for the boundary-layer displacement thickness used to determine the upper boundary. The enhanced pressure drop near the downstream boundary is due to inaccuracies in the outflow boundary condition.

Mean velocity profiles at several streamwise stations are compared with the experimental data in Figure 3. The first station is on the flat inlet section, eight boundary-layer thicknesses ahead of the curved section. The next four stations are at 15, 30, 45, and 60° (4.7, 9.5, 14.2, and 18.9 boundary-layer thicknesses into the curved section). The velocity data are normalized with the velocity profile that would be developed by an inviscid flow through the curved section. To a good approximation, this profile varies linearly according to

$$U_p(y) \simeq U_{pw}(1 + y/\mathrm{R}) \tag{1}$$

where $U_{pw}$ is the inviscid velocity that would be achieved at the wall. Overall, the agreement between simulation and experiment is quite good. On the flat section, the simulation produces profiles that are slightly more full near the wall as compared with the experiment. This discrepancy was found to diminish with increasing mesh resolution in the streamwise and spanwise directions. The present mesh should be fine enough to capture the important large-scale turbulent structures and the reason for improved results with increasing resolution is not clear. It is difficult to ascertain whether the problem arises from the limited resolving power of the second-order method, or from inaccuracies in the subgrid-scale model; refining the mesh increases the resolution, but at the same time reduces the impact of the subgrid-scale model. In any case, the current level of agreement is deemed acceptable and detailed simulations were not performed on finer meshes.

The mean velocity profile is seen to come into better agreement with the experimental data on the curved section. Note the difference in the shape of the profile between the flat and 60° stations (first and last curves in Figure 3). The effect of concave curvature is to create fuller profiles, especially close to the wall. This is due to enhanced mixing resulting from the effects of curvature.

Reynolds shear stress profiles are shown as the solid lines in Figure 4 (the dashed lines are described below). The agreement

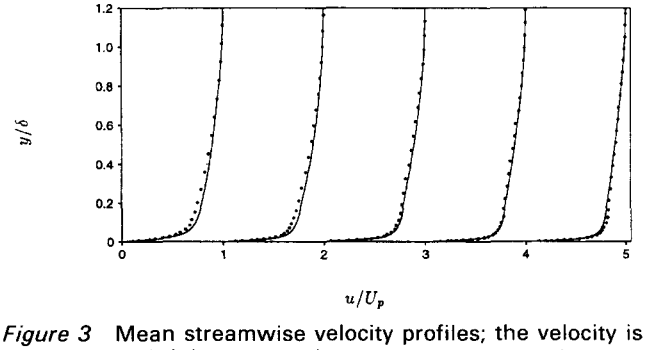


*Figure 3* Mean streamwise velocity profiles; the velocity is scaled by $U_p(y)$ (Equation 1), the streamwise profile that would be developed in an inviscid flow through the curved section; the first station is on the flat inlet section, eight boundary-layer thicknesses ahead of the curve; the next four stations are at 15, 30, 45, and 60°, respectively; ——, LES; ●, Johnson and Johnston (1989).

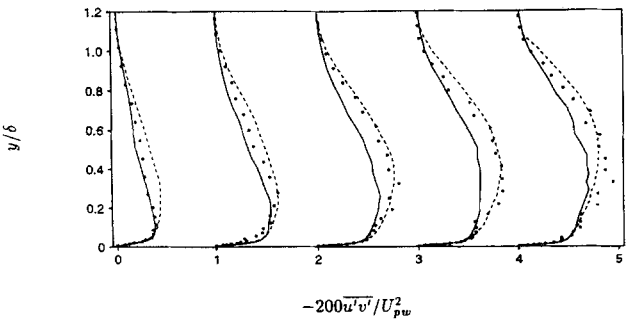


*Figure 4* Reynolds shear stress profiles; ——, LES, spatially evolving boundary layer inflow data; ----, LES, rescaled parallel flow boundary layer inflow data; ●, experimental measurements of Johnson and Johnston (1989); the first station is on the flat inlet section, eight boundary-layer thicknesses ahead of the curve; the next four stations are at 15, 30, 45, and 60°, respectively; $U_{pw}$ is an extrapolation of the core velocity to the wall assuming an inviscid profile

with the experimental data is reasonable with the simulation doing a good job of capturing the qualitative changes to the shear-stress profile that result from concave curvature. The peak Reynolds stress increases and the profile develops a bulge in the central region. On a quantitative level, however, the simulation tends to underpredict the peak Reynolds stress, especially at the 45° and 60° stations. The reason for this discrepancy is not fully understood, but there is some evidence to suggest that it is related to the details of the inflow conditions. An example of the sensitivity to inflow conditions is shown by the dashed lines in Figure 4, where an alternative set of inflow data is used. In this case, inflow data are generated in a parallel-flow boundary-layer simulation where a periodic boundary condition is applied in the streamwise direction and a no-stress, no-normal, flow boundary condition is applied on the boundary opposite the wall (at the boundary-layer edge). To increase the efficiency of the inflow generation, a very short streamwise length is used (two boundary-layer thicknesses). The parallel-flow simulation produces a mean and velocity fluctuation profiles that differ from what is expected for a spatially evolving boundary layer. In an attempt to correct for this, the inflow data are modified by rescaling the mean and vertical velocity fluctuation profiles, so that they match the experimental data taken on the flat section upstream of the curve. The rescaling operation is not sufficiently accurate to keep the boundary layer in equilibrium, and a transient develops near the inflow boundary. This effect is clearly visible in Figure 4 where the Reynolds stress is overpredicted at the first measurement station. Evidently the slightly different distribution of Reynolds stress on the flat section can lead to considerable changes in the profiles downstream. This situation is quite opposite to the behavior of a zero-pressure gradient boundary layer on a flat surface, where perturbations decay with streamwise distance. Indeed, the profiles from the two sets of inflow data continually converge toward one another on the flat entry section and are actually in much closer agreement at the start of the curve than at the first station plotted in Figure 4 (which is eight boundary-layer thicknesses upstream of the curve). Thus, the differences in the Reynolds stress profiles in the curved section is not simply an offset effect where the surplus stress on the flat section merely persists downstream. As the flow proceeds in the curved section, the profiles again separate, with the parallel-flow inlet data simulation showing a greater amplification rate. This effect is visible through a comparison of the second, third, and fourth profiles in Figure 4.

The reason for the more efficient amplification in the case of the parallel-flow inlet data is not completely understood, but there is some evidence to suggest that it is related to an artificially high degree of streamwise coherence in the inflow data resulting from application of the periodic boundary condition over a short length in the streamwise direction. This, detail is discussed further in the following section.

Velocity fluctuations are compared with the experiment in Figure 5. Once again, agreement with the experimental data is good and the qualitative changes to the profiles resulting from concave curvature are well reproduced. A bulge develops in the central portion of each profile, and it is most pronounced for the wall-normal and spanwise fluctuations. On a quantitative level, minor differences exist between the simulation and experiment. Except for the near-wall region of the streamwise profile, all three velocity fluctuations are generally underpredicted in the simulation. The reason for this discrepancy is not completely understood, but as in the case of the Reynolds shear stress, it is sensitive to the inflow conditions. Again, slightly better agreement with the experimental data is obtained when the parallel-flow boundary-layer data are used at the inlet. The velocity fluctuations are also slightly too anisotropic near the wall; the streamwise fluctuation is overpredicted; whereas, the wall-normal and especially spanwise fluctuations are underpredicted. This is a common symptom of marginal resolution in either a direct or large-eddy simulation. It is caused by an inability to

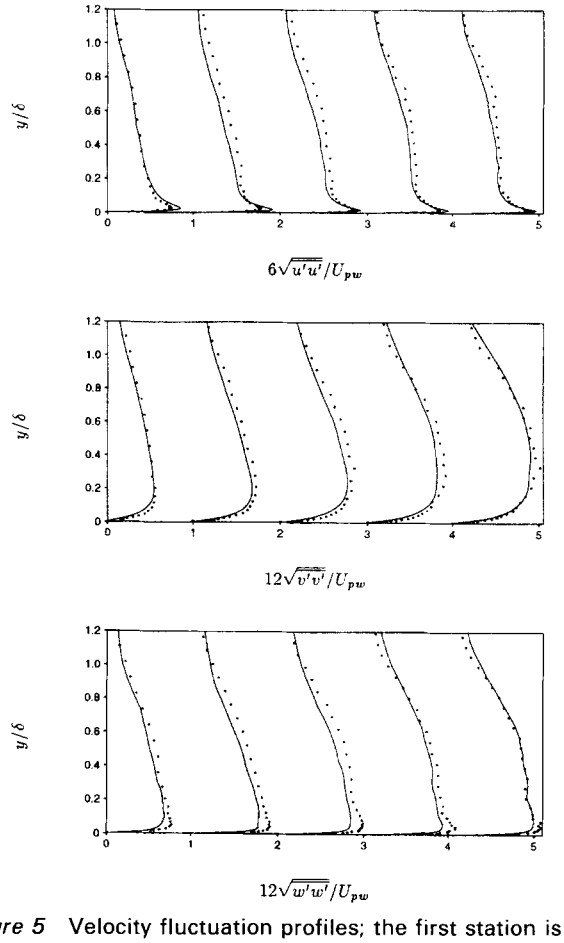


*Figure 5* Velocity fluctuation profiles; the first station is on the flat inlet section, eight boundary-layer thicknesses ahead of the curve; the next four stations are at 15, 30, 45, and 60°, respectively; $U_{pw}$ is an extrapolation of the core velocity to the wall assuming an inviscid profile; ——, LES; ●, experimental measurements of Johnson and Johnston (1989)

resolve the intercomponent energy transfer mechanism in this region of the flow. As in the case with the mean velocity profile, it was found that the discrepancy in anisotropy level could be improved by increasing the number of grid points. Once again, it is not clear whether this is a shortcoming of the second-order method or the subgrid-scale model.

The calculated skin friction is compared with experiment in Figure 6. The skin friction is seen to increase significantly due to the effects of concave curvature. The simulation captures this trend but also exhibits some quantitative differences with the experimental data. The simulation results agree best with the experiment on the flat section ahead of the curve, and beyond about 45° in the curved section. In the intermediate section, the simulated skin friction appears to respond more rapidly than the experiment as the flow enters the curved section. The small excursion immediately upstream of the curved section is due to the residual pressure gradient in this region (see Figure 2). Skin friction was determined in the experiment by fitting a log-law to the velocity profiles (Clauser chart approach). This method is accurate for equilibrium boundary layers but can be in significant error when applied in nonequilibrium situations. Since the boundary layer is displaced from equilibrium while transitioning from the flat to curved sections, the experimental skin friction measurements could be in error. To assess this possibility, skin friction was determined from the simulation data indirectly through use of the Clauser chart. The results of these measurements are shown as the triangles connected with a dashed line in Figure 6. Indeed, there are significant differences between the direct measurement and the Clauser method near the onset of curvature. In particular, the Clauser method measurements fall below the direct measurements near the onset of curvature and are actually in better agreement with the experimental data in this region. As the boundary layer comes into equilibrium farther downstream, the Clauser and direct measurements appear to be converging.

## Visualization of Taylor–Görtler structures

In the experiments of Barlow and Johnston (1988) and Johnson and Johnston (1989), the Taylor–Görtler vortices were visualized indirectly by observing the effect of their induced velocities. This was done by injecting colored dye through spanwise slits in the wall on the curved portion of the test section. Due to the upwash and downwash motions present between the vortices, the dye developed a pattern where it was ejected away from the wall in the upwash regions and confined near the wall in the downwash regions. Plumes of dye created by the upwash were visible in either a plane or cross-sectional view. Both Barlow and Johnston

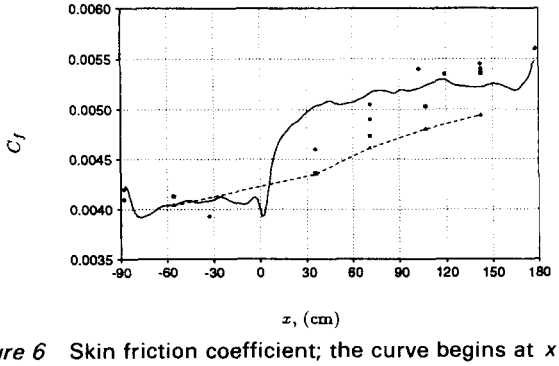


*Figure 6* Skin friction coefficient; the curve begins at $x=0$; ——, LES, direct method; ●, experimental data of Johnson and Johnston (1989); ■, experimental data of Barlow and Johnston (1988); ▲, LES, Clauser method

and Johnson and Johnston report that the dye patterns were variable in space and time, with an average streamwise coherence of about three–five boundary-layer thicknesses. At the same time, they noticed a slight preference for the vortex locations and a small systematic spanwise variation in their mean statistics.

In the simulations, the Taylor–Görtler vortices were visualized in a more direct manner through an analysis of the velocity field. This approach is complicated by the fact that the vorticity distribution in the Taylor–Görtler structures is quite diffuse, and the circulation is very low; Barlow and Johnston report that an average vortex does not even complete one revolution over the course of its lifetime. Due to the diffuse nature as well as the limited streamwise extent, Barlow and Johnston prefer not to characterize the structures as vortices. Instead, they advocate the term "roll-cells" to indicate a weak circulating motion similar to what is often found in thermal convection. Visualizing such a structure is difficult, since the induced velocities are generally smaller than the background turbulent fluctuations. Simple contour plots of quantities such as instantaneous velocity or vorticity imaged in cross-flow (spanwise-wall-normal) planes failed to depict any large-scale structure. To emphasize structures with streamwise coherence, the velocity field was first averaged over several boundary-layer thicknesses in the streamwise direction. Contour plots of the velocity components from the averaged field provided some evidence of structure, but it was found that a 2-D stream function in the cross-flow plane provided a much more clear picture of the flow pattern.

Sample contour plots are shown in Figure 7. As reported in the experiments, the flow patterns are found to be variable in space and time, with the number of vortices varying between two and eight. The fields with a large number of vortices usually contain two layers, one near the wall and another farther out in the core region. Despite the variability in flow pattern, there are some systematic differences in the flow fields which correlate with the type of inflow data used. Figure 7(a) shows a typical pattern for the case with the parallel-flow boundary-layer inlet data. Fields from this simulation usually contain two large-scale vortices that are rather coherent in the streamwise direction. In contrast, Figure 7(b) shows a typical pattern from the case with spatially-evolving inlet data. The structures found in this simulation vary considerably and are generally less coherent in the streamwise direction. In addition, the magnitude of the induced velocity is usually about a factor of two to five less in the case with the spatially-evolving boundary layer inlet data.

The differences in vortex structure and strength between the two simulations may explain the differences in Reynolds stress shown in Figure 4. In particular, the more coherent, stronger vortices in the simulation with parallel-flow boundary-layer inlet data are probably responsible for the higher levels of Reynolds stress. The reason for the higher degree of organization of structure in this case is not clear, but it may be related to the manner in which the in-flow data were generated. Specifically, the parallel-flow data were generated with a periodic boundary condition applied to a domain only two boundary-layer thicknesses long in the streamwise direction. This artificial constraint tends to promote structures with a high degree of streamwise coherence. Indeed, it was found that the near-wall streamwise vortices in this set of inflow data are unusually well organized, and it may be these structures that are more efficiently amplified in the curved section. In contrast, the spatially evolving inflow data was generated on a domain more that twelve times longer in the streamwise direction and made use of a milder periodic boundary condition applied to the flow variables in a transformed similarity coordinate. Structures in this inflow simulation decorrelate over the streamwise length, and consequently any vortices that might "seed" the downstream development of Tay-

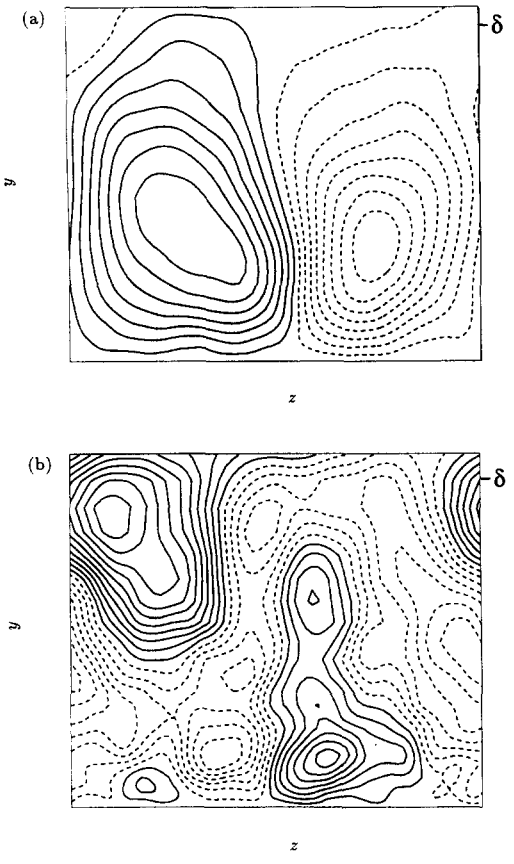


*Figure 7* Visualization of Taylor–Görtler vortices; contours of the 2-D stream-function for motion in the cross-flow plane; in order to emphasize structure with streamwise coherence, the velocity field was first averaged in the streamwise direction from the 30° station to the exit (roughly 12 boundary-layer thicknesses); (a) from the simulation with parallel-flow boundary layer inlet data; (b) from the simulation with spatially evolving boundary-layer inlet data; the local boundary-layer thickness is indicated in the upper right-hand corner of each figure

lor–Görtler cells are distributed more randomly in space and time.

## Conclusions

Large-eddy simulations of a concave-wall boundary layer have been performed. The simulations make use of the dynamic subgrid-scale model which requires neither the tuning of model constants, nor the use of ad hoc corrections for curvature. Concave curvature results in large changes to the turbulent statistics, and LES does a good job of predicting the transition from a flat wall to a concave surface. Some quantitative differences exist between the LES results and the experimental data, and these can be attributed in part to the details of the turbulent data supplied at the inflow boundary. In the experiment, streamwise vorticity is generated by the flow-conditioning-devices and is amplified in the contraction leading to the channel. These vortices may act as effective nuclei for the rapid development of Taylor–Görtler vortices in the curved section and may also partially fix their location. Indeed, Barlow and Johnston (1988) report that the vortices in their experiment have preferential locations and that the mean statistics exhibit a slight modulation in the spanwise direction with a wavelength roughly corresponding to the observed vortex spacing. The amplification of existing structures may make it difficult for simulations to match exactly a given set of measurements unless the details of the flow upstream are known and can be reproduced in the calculation. An example of this uncertainty was illustrated here where two different sets of inflow data lead to considerably different results in the curved section. It was found that the simulation with the parallel-flow boundary-layer inlet data produces second-order statistics that are in better agreement with the experimental data when compared with the simulation using spatially evolving boundary-layer inlet data. This is interesting, since the parallel-flow inlet data contain structures with an artificially high degree of streamwise coherence as a result of a periodic boundary condition applied over a very short streamwise length. It is possible that these structures act in much the same way as those generated by the flow-conditioning device in the experiment. In any case, the parallel-flow boundary layer inlet data lead to large-scale Taylor—Görtler vortices similar to those observed in the experiments. On the other hand, the simulation using spatially evolving boundary-layer data produces lesser-organized structures that are generally weaker in magnitude. These findings suggest that it may be necessary to "seed" the inflow data with some type of coherent structure in order to mimic the structures present in either a laboratory experiment or device with non-negligible free-stream disturbance level. Furthermore, it seems likely that devices that operate in quiet environments (such as free-flight) may develop flow patterns that differ from a prototype that is tested in an internal-flow experimental facility.

## References

Akselvoll, K. and Moin, P. 1993. Application of the dynamic localization model to large-eddy simulation of turbulent flow over a backward-facing step. In *Engineering Applications of Large-Eddy Simulations*, S. A. Ragab and U. Piomelli (eds.), presented at the ASME fluid engineering conference, Washington DC, June 20–24, 1993

Barlow, R. S. and Johnston, J. P. 1988. Structure of a turbulent boundary layer on a concave surface. *J. Fluid Mech.*, **191**, 137–176

Choi, H., Moin, P. and Kim, J. 1993. Direct numerical simulation of turbulent flow over riblets. *J. Fluid Mech.*, **255**, 503–540

He, J. and Song, C. C. S. 1993. Some applications of large-eddy simulation to large-scale turbulent flows at small Mach number. In *Engineering applications of large eddy simulations*, S. A. Ragab and U. Piomelli (eds.), presented at the ASME fluid engineering conference, Washington DC, June 20–24, 1993

Johnson, P. L. and Johnston, J. P. 1989. The effects of grid-generated turbulence on a flat and concave turbulent boundary layer. Report MD-53 Thermosciences Division, Dept. of Mech. Eng., Stanford University, Stanford, CA

Spalart, P. R. 1988. Direct simulation of a turbulent boundary layer up to $R_\theta = 1410$. *J. Fluid Mech.*, **187**, 61–98

Wu, X., Squires, K. D. and Lund, T. S. 1995. Large-eddy simulation of a spatially-developing boundary layer. In *Proc. of the 1995 ACM/IEEE Supercomputing Conference*, San Diego, CA, Dec. 3–8, 1995, (Available on line at http://www.supercomp.org/sc95/proceedings)

Zang, Y., Street, R. L. and Koseff, J. R. 1993. A dynamic mixed subgrid-scale model and its application to recirculating flows. *Phys. Fluids A.*, **5**, 3186–3196